

Angle-dependent electron confinement in graphene moiré superlattices

Francisco Sánchez-Ochoa[✉], Andrés R. Botello-Méndez[✉], and Cecilia Noguez^{✉*}

Instituto de Física, Universidad Nacional Autónoma de México, Apartado Postal 20-364, Ciudad de México C.P. 01000, Mexico



(Received 21 November 2020; revised 28 April 2021; accepted 4 August 2021; published 17 August 2021)

In graphene moiré superlattices, electronic interactions between layers are mostly hidden as band structures get crowded because of folding, making their interpretation cumbersome. Here, the evolution of the electronic band structure as a function of the interlayer rotation angle is studied using density functional theory followed by unfolding bands and then comparing them with their corresponding individual components. We observe interactions in regions not theoretically elucidated so far, where for small interlayer angles, gaps turn into discretelike states that are evenly spaced in energy. We find that $V_{pp\sigma}$ attractive interactions between out-of-plane orbitals from different layers are responsible for the discretization. Furthermore, when the interlayer angle becomes small, these discrete, evenly spaced states have energy differences comparable to graphene phonons. Thus they might be relevant to explain electron-phonon-assisted effects, which have been experimentally observed in graphene moiré superlattices.

DOI: [10.1103/PhysRevB.104.075430](https://doi.org/10.1103/PhysRevB.104.075430)

I. INTRODUCTION

The vertical stacking of any two-dimensional (2D) layered materials, such as graphene (G), transition metal dichalcogenides, hexagonal boron nitride, or layered oxides [1], has led to a new research field with exciting phenomena and potential applications [2]. These atomic 2D films are known as van der Waals heterostructures, following the weak-forces nature that maintains the layers together. This weak interaction suggests that the combined 2D systems' electronic properties could be a simple superposition [3]. However, recent studies that focused on atomic bilayers have shown that the physical properties can be drastically modified because of the interlayer interaction, which additionally can be modulated with the relative angle between layers [4–15].

A lattice mismatch occurs when two G layers are vertically stacked with a different crystallographic orientation between them. When a periodicity appears upon stacking, a superlattice arrangement arises with a characteristic moiré pattern [16]. The interference effect between the two layers with slightly different orientations, i.e., a minimal interlayer angle, generates moiré patterns with long wavelengths. Thus a graphene moiré superlattice or cell is a periodic 2D material composed of twisted-bilayer G (TBLG). Here, new physical effects arise from the interlayer potential modulation that depends on the relative orientation. Moiré patterns are composed of local combinations of vertical atomic arrangements AA and AB (BA)—these latter have zero interlayer angles—and sequences between them. The arrangement fluctuations modulate the interlayer potential and, consequently, the electronic band structure of TBLG [17–19]. In AA arrangements, the atoms in both layers are precisely aligned, while in AB (BA) arrangements, the atoms of one layer lie directly on the center

of a hexagon in the lower (upper) graphene sheet. The AB order is also known as Bernal stacking, and it is more stable than the AA-stacked bilayer [20]. Density functional theory (DFT) and semiempirical tight-binding studies have shown that AA and AB arrangements show different electronic behavior near the Fermi level (E_F), while at lower energies their bands are quite similar [20].

Experimental results obtained using different characterization techniques, such as scanning tunneling microscopy (STM), Raman spectroscopy, and angle-resolved photoemission spectroscopy (ARPES), among others, have shown that TBLGs exhibit band structures different from the isolated layer [14,21–26]. This suggests an interlayer coupling that modifies the electronic band structure near E_F , leading to distinct novel electronic and optical properties compared with the isolated G layer [3,27,28]. Some exciting results include van Hove singularities (VHSs), minigaps in the far-infrared region, a decrease in charge-carrier velocity near the Dirac point, the so-called moiré bands, localization of Dirac electrons, and stacking-dependent optical and conduction properties, together with an angle-controlled optical activity, among others [3–16,20–28].

In this paper, the evolution of the electronic band structure as a function of the interlayer rotation angle θ in graphene moiré superlattices (GMSs) is studied. We employed a methodology that allows us to elucidate the physical effects of the mutual interactions between 2D layers by unfolding the electronic bands of systems with double periodicity [29]. In particular, the combination of total energy DFT calculations followed by the unfolding approach permits us to obtain effective electronic bands (EEBs) projected onto the isolated G primitive cell. Then, the EEB allows us to give a direct physical interpretation of the electronic changes that a G layer suffers when interacting with a second sheet. Applying the above methodology, we identify many energy band gaps at about 2 eV, above and below E_F , close to \mathbf{M} , and around a

*Corresponding author: cecilia@fisica.unam.mx

well-defined energy window. These states exhibit a discrete-ladder-like behavior at small interlayer angles induced by the electronic degeneration breaking, caused by $V_{pp\sigma}$ interactions between π -band electrons from each layer. At lower energies and around Γ , a band splitting is found by inspecting the EEB. At different energies and reciprocal \mathbf{k} points, all these electronic effects are associated with angle-modulated interactions between the out-of-plane orbitals of both G layers that form the π bands. Additionally, we can easily reproduce and identify the Dirac cone interactions between layers, which are recognized as van Hove singularities that move toward E_F as θ decreases. This effect has been observed experimentally and theoretically [14,23,28].

While the band structure of TBLG has been extensively studied, most of the efforts have focused on the spectrum related to low-energy excitations. Indeed, in this region, one can approximate the proper TBLG band structure near E_F , which can shed light on transport properties. However, this paper goes beyond this region, analyzing the effects on the band structure at lower energies when stacking two graphene layers with different relative angles. The main original result is how the states farther away from the Fermi level start hybridizing. The character of the hybridization is not trivial and cannot be explained by Bragg diffractions. Instead, the formation of localized states is a direct consequence of the interlayer interaction. The results discussed here provide a precise physical analysis of the electronic band structure evolution of TBLG as a function of the relative angle between layers, where discrete evenly spaced states and band splitting are observed, besides the well-known Dirac cone interactions and variation of the charge-carrier group velocity.

II. METHODS

A. TBLG structures

Commensurate GMSs or TBLG are labeled with two integer indices (m, n) associated with the G-primitive-cell lattice vectors on each layer. The (m, n) indices are used to construct TBLG systems, as well as the matrix transformation, \mathbf{P} , used in the unfolding method [29]. Structural parameters such as θ ($^\circ$), the interlayer rotation angle; N , the total number of carbon atoms in the GMS; a_{sc} , the superlattice cell parameter; and R , the reconstruction factor, are calculated as in Ref. [30] using the following expressions:

$$\theta = \cos^{-1} \left[\frac{m^2 + 4mn + n^2}{2(m^2 + mn + n^2)} \right] * \left(\frac{180}{\pi} \right), \quad (1)$$

$$N = 4(m^2 + n^2 + mn), \quad (2)$$

$$a_{sc} = a_{PC} \sqrt{|\det \mathbf{P}|}, \quad (3)$$

$$R = \sqrt{|\det \mathbf{P}|} \times \sqrt{|\det \mathbf{P}|}, \quad (4)$$

respectively. Here, m and n are integer numbers that characterized the commensurate GMS, where $m \geq n$. Also, $a_{PC} = 2.44 \text{ \AA}$ is the lattice constant of the optimized G primitive cell, \det means the determinant of a matrix, and \mathbf{P} is the matrix used in the linear transformation between primitive-cell and supercell (SC) lattice vectors, according to Ref. [29]. Here, we

TABLE I. Structural parameters of a GMS defined with (m, n) , θ , relative angle; N , number of carbon atoms in the supercell with a lattice constant a_{sc} and reconstruction factor R . After optimization: d , average distance between layers; Δ , average atomic corrugation.

(m, n)	θ (deg)	N	a_{sc} (Å)	R	d (Å)	Δ (mÅ)
(2,1)	21.78	28	6.45	$\sqrt{7} \times \sqrt{7}$	3.28	1.89
(4,2)	21.78	112	12.91	$2\sqrt{7} \times 2\sqrt{7}$	3.28	2.44
(5,3)	16.42	196	17.07	7×7	3.28	16.36
(3,2)	13.17	76	10.63	$\sqrt{19} \times \sqrt{19}$	3.26	23.89
(6,4)	13.17	304	21.27	$2\sqrt{19} \times 2\sqrt{19}$	3.29	26.86
(7,5)	10.99	436	25.47	$\sqrt{109} \times \sqrt{109}$	3.31	37.33
(4,3)	9.43	148	14.84	$\sqrt{37} \times \sqrt{37}$	3.29	40.18
(5,4)	7.34	244	19.05	$\sqrt{61} \times \sqrt{61}$	3.30	61.01
(6,5)	6.01	364	23.27	$\sqrt{7} \times 13 \times \sqrt{7} \times 13$	3.30	69.12
(7,6)	5.09	508	27.49	$\sqrt{127} \times \sqrt{127}$	3.30	69.82
(9,8)	3.89	868	35.94	$\sqrt{7} \times 31 \times \sqrt{7} \times 31$	3.31	72.19
(11,10)	3.15	1324	44.39	$\sqrt{331} \times \sqrt{331}$	3.29	74
(13,12)	2.64	1876	52.84	$\sqrt{7} \times 67 \times \sqrt{7} \times 67$	3.32	72.17

study TBLG or the commensurate GMS with (m, n) listed in Table I.

B. DFT calculations

Total energy DFT calculations were performed using the SIESTA code [31,32]. The exchange-correlation energy was described by a van der Waals (vdW) [33] functional using the Klimeš, Bowler, and Michaelides parametrization [34]. The electron-ion interactions are treated with norm-conserving pseudopotentials [35]. A linear combination of pseudoatomic orbitals (LCAO) is employed to expand the valence electronic states, with an optimized double- ζ polarized (DZP) basis set. An energy mesh cutoff of 500 Ry is applied to sample the electronic density in the real space. The electronic self-consistency was converged to a value of 10^{-5} . The Monkhorst-Pack scheme [36] is used to sample the Brillouin zone (BZ) with an optimal $21 \times 21 \times 1$ grid for the smallest SC. The atomic optimization was carried out with the conjugate gradient algorithm with a maximum value in the interatomic forces of 0.01 eV/\AA . Energy cutoff and k -grid convergence tests are performed on the systems leading to the values above as the optimal ones. To simulate a GMS, we employ the SC method with a vacuum space of 25 \AA between the adjacent G monolayers to avoid spurious interactions. The interlayer angle between G monolayers takes a reference to the zigzag directions of each sheet, as reported in Ref. [30]. Since both G sheets have hexagonal symmetry, the maximum limit of the rotation angle is $\theta = 30^\circ$. Visualization of atomic models and isosurfaces is performed using VESTA [37].

C. Unfolding method

We employ a general unfolding method for the electronic bands of systems with double periodicity that let us elucidate the physical effects of the mutual interactions between systems. The method is based on DFT with a linear combination of atomic orbitals as a basis set and considers two symmetry operations of the primitive cell: A standard expansion and

a single rotation. As a result, the unfolding method enables us to study the electronic properties of vertically stacked homostructures or heterostructures. The details of the unfolding approach are discussed in Ref. [29]. Briefly, the unfolding method follows the next steps: (i) The electronic band structure is calculated in the BZ of the SC, and then it is projected into the reciprocal space of the primitive cell, i.e., eigenvalues and eigenfunctions, $E(\mathbf{k})$, $\psi_I(\mathbf{k}, \mathbf{r})$, where I labels the different bands. (ii) Then, we identify the equivalent atoms between the extended and primitive cells, which allows us to determine the corresponding eigenfunctions, which are orthonormalized. (iii) Next, we project the extended-cell eigenfunctions onto the primitive-cell ones using the transformation matrix \mathbf{P} and then calculate the spectral weights $W(\mathbf{k}, I)$. (iv) Finally, the effective electronic band (EEB) is obtained along a path that contains the high-symmetry points of the BZ of the primitive cell. The spectral weights $W(\mathbf{k}, I)$ determine how much of the pristine G electron state is preserved when interacting with a second layer. Thus $W(\mathbf{k}, I) = 1$ means that the G electronic state is fully recovered, while $W(\mathbf{k}, I) = 0$ indicates that it is absent. Meanwhile, $W(\mathbf{k}, I) < 1$ suggests an alteration of the electronic state because of the interlayer interaction. In this way, the EEB compares directly to the band structure of pristine G. [This latter and its density of states (DOS) are shown for reference in Fig. 6 in Appendix A for completeness.] This method opens the possibility to directly compare with experiments (for example, ARPES spectra), which otherwise would be impossible to distinguish.

III. RESULTS AND DISCUSSION

A. Structure of TBLG as a function of θ

Let us start discussing the structural parameters of TBLGs upon full optimization using SIESTA [31,32]. We first consider an AA stacking pattern with $\theta = 0^\circ$, followed by a rotation between layers. TBLG superlattices exhibit AA, AB, and BA stacking patterns in different regions. These three patterns are indicated with green, yellow, and orange circles, respectively, in the upper panels of Fig. 1. Here, top views for (9,8) [Fig. 1(a)] and (7,5) TBLGs [Fig. 1(b)] are shown. Their corresponding isometric views are shown in the bottom panels, where they are scaled up 10 and 50 times, respectively, to make visible the atomic corrugation after optimization. From the isometric views, sinusoidal patterns in the atomic corrugation Δ are found, with separation maxima in AA-stacking domains and minima in AB- or BA-stacking ones. This sinusoidal behavior of Δ has the same periodicity as the moiré superlattice and agrees with previous reports [38]. The number of AA, AB, and BA domains increases as $\theta \rightarrow 0^\circ$. However, when $\theta = 0^\circ$, only the AA stacking is present, and a null corrugation is observed. The quantified average distances, d , between monolayers present variations smaller than 2% as a function of the angle. However, Δ increases nearly two orders of magnitude as θ goes to zero, being smaller than 100 mÅ in all cases. Notice that TBLG with different (m, n) may have the same relative angle but different N , a_{SC} , and R , where all these parameters are related by an integer factor. For example, TBLGs (2, 1) and (4, 2) in Table I have the same $\theta = 21.78^\circ$, while $N_{(4,2)} = 4N_{(2,1)}$, etc. However,

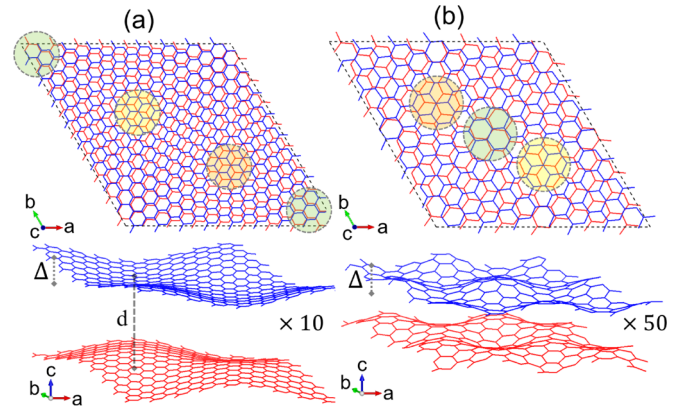


FIG. 1. Optimized TBLG models: (a) (9,8) and (b) (7,5). Red and blue lattices represent the bottom and top G layer, respectively. Upper panels show the top views, where AA, AB, and BA domains are indicated with green, yellow, and orange circles, respectively. Bottom panels show isometric views scaled up (a) 10 and (b) 50 times. Δ is the atomic corrugation, and d is the average difference of the vertical coordinate on each G layer.

independently of N , TBLGs (2, 1) and (4, 2) have the largest θ but the smallest Δ because they have exactly the same moiré pattern. In this case, the in-plane relaxation is about 0.001 Å, which is negligible.

B. Effective electronic bands in TBLG

To discuss the electronic properties, we illustrate the unfolding method used here for TBLG (2,1) with $\theta = 21.78^\circ$. Notice that TBLGs with the same twist angle but different (m, n) have identical electronic properties, as expected. The BZ corresponding to SC and the BZs of the top and bottom G primitive cells are shown in Fig. 2(a) as green, red, and blue hexagons. For each BZ, its high-symmetry points, \mathbf{K} and \mathbf{M} , are indicated with the corresponding color; Γ is the same in all BZs. Figure 2(b) shows the electronic bands of the SC along the path shown as dashed green lines in Fig. 2(a), $\Gamma \rightarrow \mathbf{K}_{\text{SC}} \rightarrow \mathbf{M}_{\text{SC}} \rightarrow \Gamma$. Electronic states from both G layers are folded into the reciprocal space of SC [39]. We can identify the linear dispersion of Dirac cones close to E_F at \mathbf{K}_{SC} , where E_F was set to 0 eV in all graphs for simplicity. However, the change in the electronic structure is hidden by the use of the SC. Consequently, it is hard to go deeper in our analysis than Fig. 2(b), because of the large number of bands due to folding.

To overcome this problem, we employ the unfolding approach described above. The left-hand side of Fig. 2(c) shows the EEB, where the size and color of the dots represent $W(k, I)$. The bands forming the Dirac cones show discontinuities with $W(k, I) < 1$, in both valence and conduction bands. Following these bands at deeper energies, a split into two bands around -8 eV toward Γ is found, with $W(k, I) \simeq 0.5$ for each one and an energy difference of ~ 1 eV. In contrast, the rest of the bands are practically unaffected, with $W(k, I) \simeq 1$. The effect of interlayer interaction on the σ bands is expected to be small because of the orthogonal character of these bands to the π bands involved in the interaction. Using the information from the total and partial DOS in the right-hand panel of Fig. 2(c), we found that the main alterations in

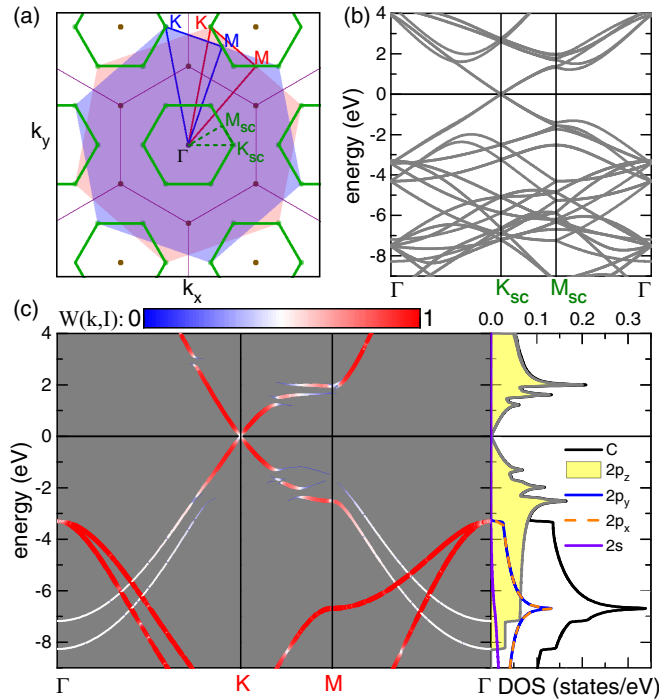


FIG. 2. TBLG (2,1) with $\theta = 21.78^\circ$. (a) The BZ of SC is shown as green solid lines, and the BZs of both G primitive cells are shown as red and blue hexagons. Their \mathbf{K} and \mathbf{M} high-symmetry points are also in green, red, and blue colors. Γ coincides for all BZs. (b) Calculated electronic bands of SC [green dashed lines in (a)]. (c) Left panel: Unfolded electronic bands or EEB of SC projected onto one G primitive cell, where $W(k, I)$ is proportional to the size and color of the dots (color bar on the top). Right panel: DOS per atom of SC, with total (black curve) and partial contributions from orbitals.

EEB are along the bands associated with $2p_z$ or out-of-plane orbitals, known as π bands. On the other hand, the unchanged bands result from $2s$, $2p_x$, and $2p_y$ or in-plane orbital combinations and are known as σ bands. Between $(-3.0, -1.5)$ eV and $(+1.2, +2.5)$ eV, significant differences in the π bands reveal peaks in the DOS above and below E_F , corresponding to those energies where π bands are broken and give origin to van Hove singularities (VHSs). At lower energies, a step-function behavior is observed in the DOS, associated with the band splitting. The half drop in the DOS at -7.1 eV is consistent with $W(k, I) = 0.5$, the spectral weight results. Note that from the electronic bands of the SC in Fig. 2(b), it is impossible to identify the origin of most VHS and DOS step functions below -7 eV, besides a few features close to E_F .

In general, we find that the π bands are perturbed; meanwhile, the σ bands remain unaffected. The alteration of the π bands is due to the electronic interaction between $2p_z$ or out-of-plane orbitals belonging to different layers. The different numbers and positions of the AA-, AB-, and BA-stacking domains found at different angles modulate the out-of-plane interactions. [To demonstrate this, in Fig. 7 in Appendix A, we show the EEB of SC TBLG (2,1) with an interlayer distance more than twice the equilibrium distance and its corresponding DOS.] Here, the electronic bands of pristine G are reproduced. Therefore we can conclude that the

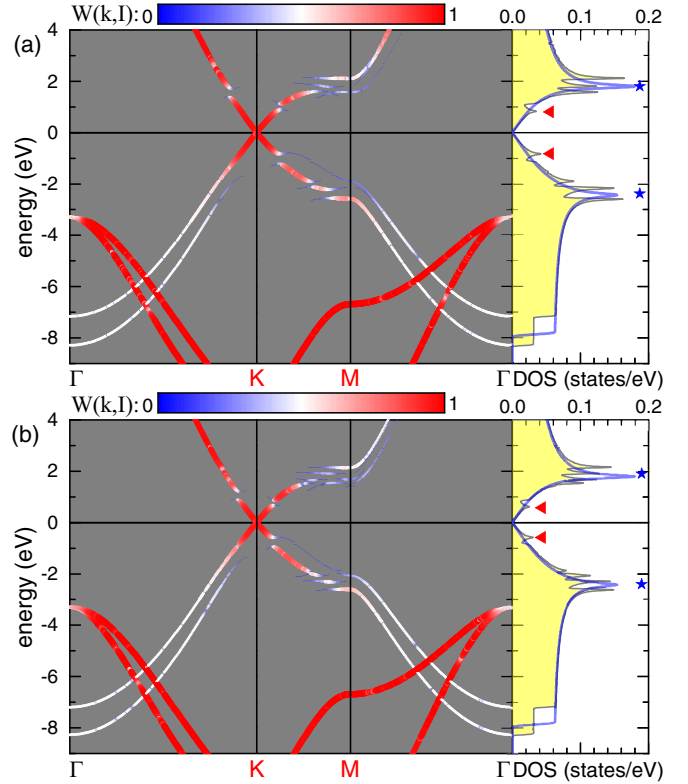


FIG. 3. EEB of TBLGs with angles (a) $\theta = 13.17^\circ$ and (3,2) and (b) $\theta = 9.43^\circ$ and (4,3). The partial DOS per atom with contributions of $2p_z$ is included (yellow), and also that of pristine G (blue curve). Red triangles mark VHSs close to \mathbf{K} and E_F , while blue stars indicate VHSs from gaps close to \mathbf{M} .

significant alterations in the π bands observed in EEB and its DOS at the equilibrium interlayer distance are caused by the electronic interaction between $2p_z$ orbitals and not because of Bragg diffractions inherent to the SC folding.

C. EEBs as a function of θ

To analyze the electronic properties' angle dependence, we consider two additional TBLGs with $\theta = 13.17^\circ$ and $\theta = 9.43^\circ$. Applying the above procedure, we calculate their EEB and DOS, shown in Figs. 3(a) and 3(b), respectively. Again, the σ bands remain unperturbed, the π -band splitting is observed around -8 eV at the Γ point, showing features quite similar to those for $\theta = 21.78^\circ$, and also the π bands exhibit clear modifications that depend on the given angle. For instance, we find quasiflatbands at about $(-3.0, -1.5)$ eV and $(+1.2, +2.5)$ eV in the \mathbf{K} - \mathbf{M} segment that give rise to π -band discontinuities and VHSs in the DOS. It is important to notice that the energies, the k points, and the number of discontinuities or gaps depend on the relative interlayer angle. For example, the gaps at low energies above and below E_F , and marked with a red triangle in the DOS plots in Fig. 3, move simultaneously toward \mathbf{K} and E_F as θ turns small. This latter result is in excellent agreement with previous experimental and theoretical reports, which identified these VHSs as the consequence of the interactions between Dirac cones

in each layer [4,14,18,28]. In Appendix B, we show our main findings for these gaps close to \mathbf{K} and E_F as a function of θ , which compare very well with previous experimental and theoretical results.

On the other hand, the minigaps around ± 2.5 eV behave differently as a function of θ . They are characterized by three and four VHSs for $\theta = 13.17^\circ$ and $\theta = 9.43^\circ$, respectively. They are closer to \mathbf{M} instead of \mathbf{K} and remain around the same energies, almost independent of the relative angle. However, as a function of θ they undergo major changes at energies around -3.0 and $+3.0$ eV and in \mathbf{K} - \mathbf{M} . The many gaps that appear around -2.5 eV for occupied states, and $+2.0$ eV for empty states close to \mathbf{M} coming from \mathbf{K} , behave differently from those that move simultaneously toward \mathbf{K} and E_F as θ turns small. In pristine G (Fig. 6 in Appendix A), we see that the π band shows saddle points at about -2.2 and $+1.8$ eV in \mathbf{M} and, consequently, VHSs in the DOS. However, in the presence of a second G layer, these bands split into many discretelike states. Furthermore, as the relative angle diminishes, more localized states appear, spreading over an energy window not larger than 1.0 eV. These states show an almost constant energy separation between successive VHS peaks [as seen in Fig. 8(a) in Appendix B], between -2.8 and -2.0 eV for occupied states and between $+1.5$ and $+2.3$ eV for empty states.

D. Origin of discrete electronic states close to \mathbf{M}

To elucidate the origin of these states, we additionally perform semiempirical tight-binding calculations. Here, $V_{pp\sigma}$ (attractive) and $V_{pp\pi}$ (repulsive) overlapping parameters of $2p_z$ orbitals in both G layers are considered. By switching these parameters on and off and looking at in-plane and out-of-plane interactions, we find that $V_{pp\sigma}$ attractive interactions between out-of-plane orbitals from different layers are responsible for the discretization. The equally spaced energy distribution between consecutive states suggests an electronic resonant behavior between layers, resembling quantum dipole oscillators observed in G quantum dots [40]. In Appendix C, we show a brief summary of the tight-binding model we employed. The interlayer interactions are observed by switching on and off in-plane and out-of-plane parameters for the electronic bands (as shown in Fig. 9 in Appendix C).

To observe these equally spaced bands, we analyze the projected states along the trajectory between both \mathbf{M} points that belong to the top and bottom G sheets. This is shown in Fig. 4(a), where red and blue colors are used to identify in which G layer the \mathbf{M} point is situated. As θ decreases, the distance between both \mathbf{M} points also does. Here, we show the projected SC states in both the top and bottom G sheets when the interlayer angle is just $\theta = 3.15^\circ$. The projection is performed along $\mathbf{A} \rightarrow \mathbf{M}_{\text{blue}} \rightarrow \mathbf{M}_{\text{red}} \rightarrow \mathbf{B}$, which corresponds to the zigzag direction in the real space, and \mathbf{A} and \mathbf{B} are shown in Fig. 4(a). Now, in Fig. 4(b), we observe two interesting features: The energy separation between flatbands is mostly even, and the location of the projected states alternates between the top and bottom layers. For instance, we find electronic states near -2.68 eV at the blue \mathbf{M} from the top layer, which are followed by states projected in the bottom layer (red) at -2.58 eV, then blue ones at -2.48 eV, and so on

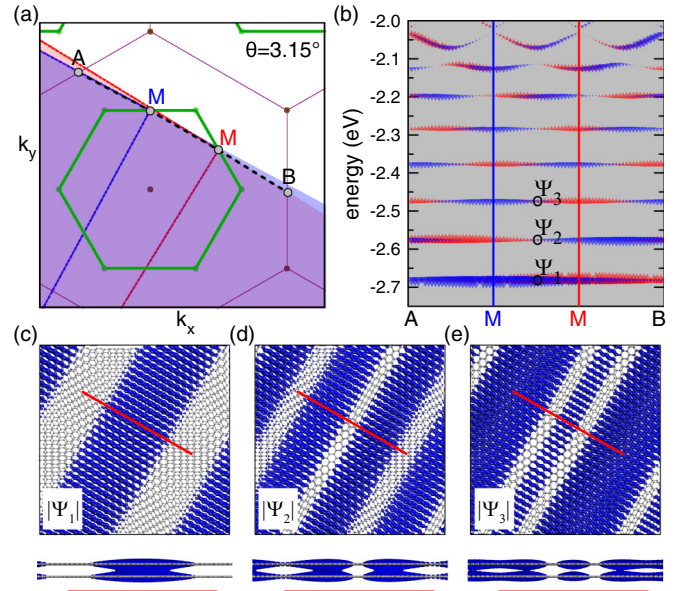


FIG. 4. (a) SC reciprocal space showing the \mathbf{M} points belonging to the top (blue) and bottom (red) G layers. (b) EEB along $\mathbf{A} \rightarrow \mathbf{M}_{\text{blue}} \rightarrow \mathbf{M}_{\text{red}} \rightarrow \mathbf{B}$ for TBLG with $\theta = 3.15^\circ$, projected at the top (blue) and bottom (red) G layers. $W(k, I)$ is proportional to triangle size. (c)–(e) Upper panels: Top views of the real space projection of $|\Psi|$ evaluated at the middle of $\mathbf{M}_{\text{blue}} \rightarrow \mathbf{M}_{\text{red}}$ for the electronic states with lower energy, as indicated in (b). Lower panels: side views of the corresponding real space projection of $|\Psi|$. The red line is ~ 40 Å and the isosurfaces are calculated with 0.01 Å^{-2} .

consecutively. In Figs. 4(c)–4(e), we show top and side views of the real space along with corresponding wave-function norms $|\Psi|$ for the indicated electronic states in Fig. 4(b). Here, we observe that while wave functions are delocalized in the armchair directions, they are finite along the red line that corresponds to the zigzag direction. Additionally, the side view shows that $|\Psi|$ are in both G layers, indicating their hybridization that allows the observed resonant behavior.

These discrete states have an energy difference of about 100 meV or smaller and are located alternately at the top and bottom layers. On the red \mathbf{M} point, an equal behavior is found when changing red to blue and vice versa. Between both \mathbf{M} points, an overlapping between projected states from both layers, resulting in an electronic hybridization or coupling between layers due to vdW interactions, is found. This latter is consistent with recent experimental observations in 1D moiré superlattices from double-wall carbon nanotubes, where an intertube coupling effect was measured [41]. It has been shown that this coupling is important for engineering the electronic structure and optical properties of moiré superlattices [42].

Finally, we discuss the relevance of θ as a new parameter for band engineering in GMSs. Upon the unfolding approach, we find new band gaps that appear below -2.0 eV and above $+1.5$ eV, which are equally spaced in energy near \mathbf{K} . Figure 5 shows EEBs along the $\mathbf{K} \rightarrow \mathbf{M}$ trajectory for different TBLGs, where discrete electronic states arise. Recall that electronic properties change drastically along this trajectory with energies around ± 2.5 eV, involving $V_{pp\sigma}$ interactions between $2p_z$ orbitals from both G layers. As θ decreases,

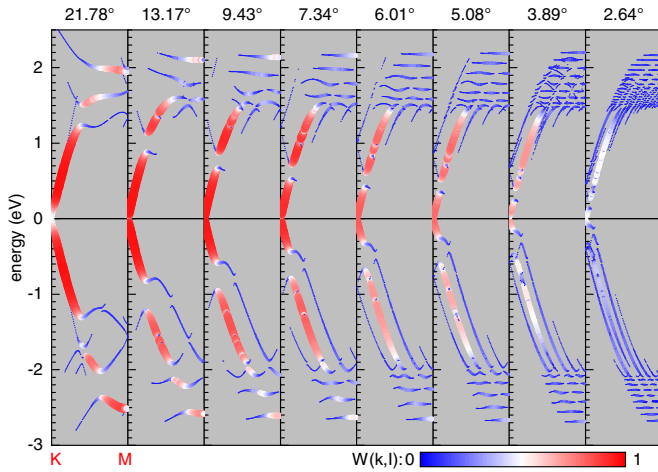


FIG. 5. EEB in **K-M** for TBLG with different angles. $W(k, l)$ is proportional to dot size and color. $E_F = 0$ eV.

these gaps turn into discrete or localized electronic states evenly spaced, resembling G quantum dots. By varying θ , the number and energy difference of these evenly spaced localized electronic states can be tuned. As the energy separation between discrete states becomes smaller than 100 meV when $\theta \rightarrow 0$, electron-phonon-driven processes are made possible. These latter might be of interest in the ultrafast absorption and emission process in the UV region [43], as well as to explain superconductivity at very small angles [44,45]. We would like to stress that this is the primary theoretical evidence using DFT: a set of flatbands emerges as discrete states because of the interaction between G layers, which can be tuned with the interlayer angle.

IV. CONCLUSIONS

The angle-dependent evolution of the electronic properties of graphene moiré superlattices is discussed within density functional theory by unfolding bands onto the graphene primitive cell. The unfolding reveals electronic changes upon addition of a second graphene sheet due to the interaction between out-of-plane orbitals ($2p_z$), forming different kinds of gaps and a band splitting. Gaps of the first kind are close to **K** and approach the Fermi level as the interlayer angle decreases. We confirm that the origin of these gaps is because of Dirac cone interlayer interactions. The second kind is given by many gaps close to **M**, where the flatband electronic degeneration is broken due to $V_{pp\sigma}$ interactions of the out-of-plane orbitals. When the interlayer angle goes to zero, these gaps turn into discretelike states, which are evenly spaced in energy with gaps around 100 meV and smaller, and increase in number. These gaps are of the order of the phonon energies of graphene, where E_{2g} is at an energy of approximately 190 meV. An interlayer coupling gives rise to such gaps, and thus they depend on the interlayer angle. Finally, at low energies in the valence and along the Γ -**K** and Γ -**M** trajectories, the band divides in two, showing a hybridization between orbitals from different layers. The results discussed here demonstrate direct evidence of the electronic discretization into highly anisotropic and well-ordered states

of graphene moiré superlattices, which can be relevant to explain electron-phonon-assisted effects recently observed in experiments.

ACKNOWLEDGMENTS

The authors acknowledge partial support from DGAPA-UNAM Grant No. PAPIIT IN109618 and CONACYT Mexico Grants No. A1-S-14407 and No. 1564464. F.S.-O. also acknowledges National Supercomputing Center at IPICYT Grant No. TKII-2020-FSO01.

APPENDIX A: UNCOVERING THE INTERACTION IN TBLG

The detailed procedure for unveiling the interaction in TBLG using the unfolding approach is described in this Appendix. Let us consider the pristine G as the reference system. The DFT-calculated electronic structure and DOS of the G primitive cell are shown in Fig. 6. Suppose now that a second layer is placed *on top* of the first, but let us neglect the layers' interaction. This can be done in a DFT calculation by placing the second layer at a distance far enough to nullify the interaction. As described in Sec. II A, under commensurate considerations, the system will form a superlattice SC characterized by indices m and n . The high-symmetry points are **K**_{SC}, **M**_{SC}, and Γ , where we have dropped the subscript for the reciprocal lattice origin since it is always the same. The band structure and density of states for a noninteracting system with ($m = 2, n = 1$) are shown as black curves in Fig. 7(a).

At the noninteracting system, the band structure going through a path that connects the high-symmetry points $\Gamma \rightarrow \mathbf{K}_{SC} \rightarrow \mathbf{M}_{SC} \rightarrow \Gamma$ is shown as black curves in Fig. 7(a). Upon projection of the eigenstates of the SC onto the orbitals of our reference G (see Eq. 2 of Ref. [29]), which can be done in a localized basis set as in this case, we obtain the spectral weights $W(\mathbf{k}, l)$. For the noninteracting case, the spectral weights are either 1 or 0, meaning that SC wave functions completely map onto the G-primitive-cell wave functions. In contrast, when considering the equilibrium interlayer distance, where

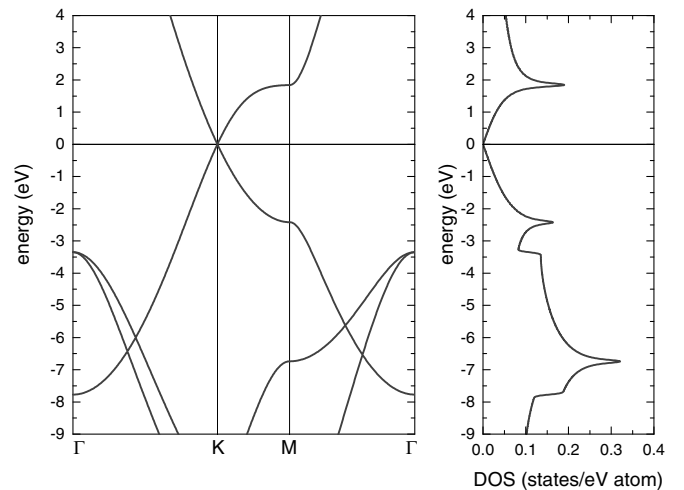


FIG. 6. Electronic bands of pristine G, as well as the DOS obtained using DFT. Here, $E_F = 0$ eV.

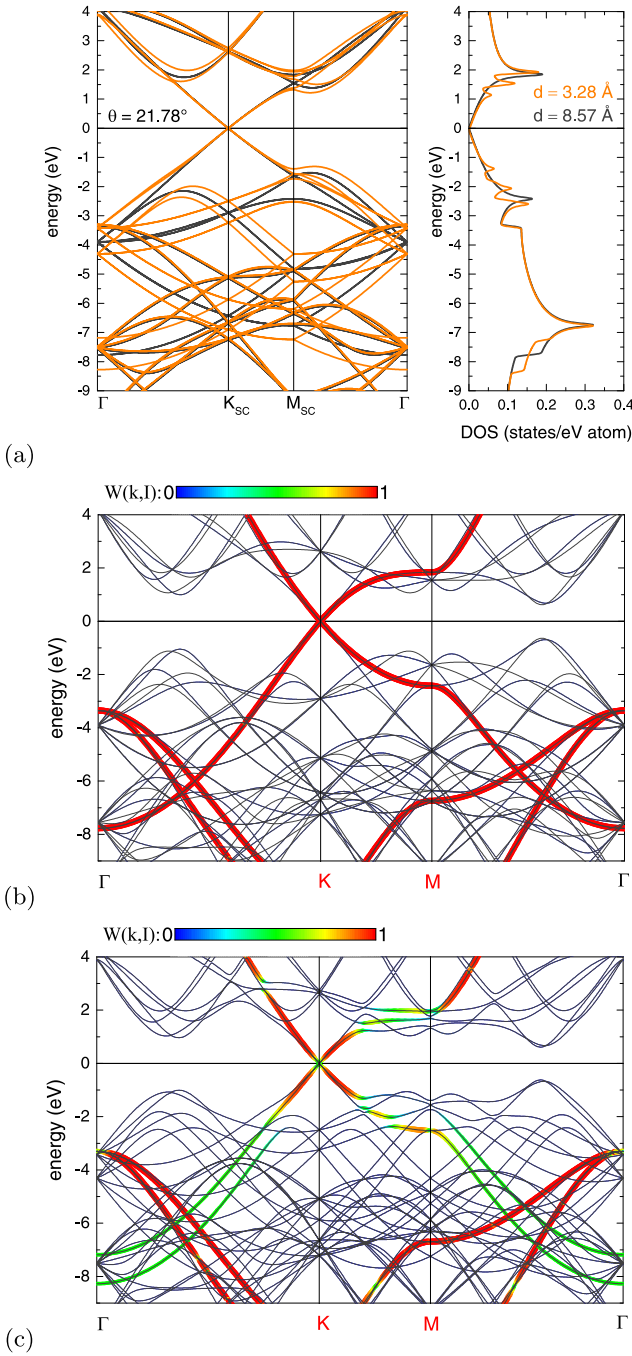


FIG. 7. (a) Electronic structure and DOS of SC TBLG (2,1) and $\theta = 21.78^\circ$ at a separation distance $d = 3.28 \text{ \AA}$, in orange, and $d = 8.57 \text{ \AA}$, in black. (b) EEB of TBLG (2,1) at $d = 8.57 \text{ \AA}$. (c) EEB of TBLG (2,1) at $d = 3.28 \text{ \AA}$. $W(k, l)$ is proportional to dot size and color, and $E_F = 0 \text{ eV}$.

the layers interact, the band structure along the SC path [Fig. 7(a), orange curves], shows significant deviations from the G discussed in this paper. The difference between the black and orange curves goes beyond the high-symmetry points, where the Bragg diffractions occur. Furthermore, the spectral weights along the $\Gamma \rightarrow \mathbf{K}_{\text{SC}} \rightarrow \mathbf{M}_{\text{SC}} \rightarrow \Gamma$ path have a full distribution of values, meaning that the mapping of the

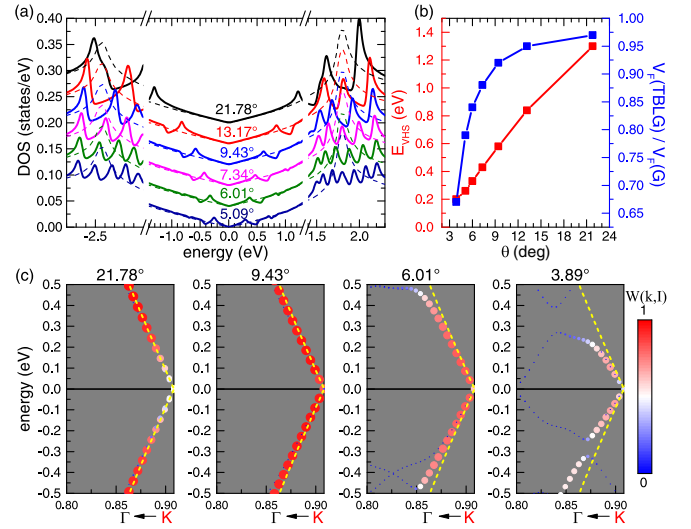


FIG. 8. (a) DOS per atom close to E_F as a function of θ . Plots are vertically shifted, and dashed curves correspond to pristine G, included for clarity. (b) E_{VHS} of the first gap below E_F , and normalized Fermi velocity, $\tilde{v}_F = v_F(\text{TBLG})/v_F(\text{G})$, as a function of θ . (c) EEB close to E_F and around \mathbf{K} for TBLG with different θ . $W(k, l)$ is proportional to dot size and color. For comparison, we plot the linear dependence of the pristine G band (dashed yellow line).

SC onto the G system is no longer perfect and the interlayer interaction caused it.

Among the effects that are easy to identify without the need of unfolding are E_{VHS} , the energies of the van Hove singularity below the Fermi level; ΔE_{VHS} , the energy difference between van Hove singularities peaks closer to the Fermi energy; and the velocity ratio, $\tilde{v}_F = v_F(\text{TBLG})/v_F(\text{G})$, of the charge carriers in the valence band. These charge-carrier velocities are calculated from the fitted slopes, as shown in Fig. 8(c). These values are in Table II, which compare well with the experimental results based on ARPES measurements in Ref. [46]. From here, we estimate a value of $E_{\text{VHS}} = 1.6 \text{ eV}$, for an

TABLE II. E_{VHS} of the first gap below the Fermi level, as well as the energy difference between occupied and empty VHSs close to the Fermi level, ΔE_{VHS} . TBLG Fermi velocity normalized with pristine G, $\tilde{v}_F = v_F(\text{TBLG})/v_F(\text{G})$, is also shown.

(m, n)	θ (deg)	E_{VHS} (eV)	ΔE_{VHS} (eV)	\tilde{v}_F
(2,1)	21.78	-1.30	2.53	0.97
(4,2)	21.78	-1.30	2.54	0.97
(5,3)	16.42	-1.02	2.01	0.96
(3,2)	13.17	-0.82	1.66	0.95
(6,4)	13.17	-0.82	1.68	0.95
(7,5)	10.99	-0.70	1.41	0.94
(4,3)	9.43	-0.59	1.19	0.92
(5,4)	7.34	-0.44	0.89	0.88
(6,5)	6.01	-0.34	0.70	0.84
(7,6)	5.09	-0.26	0.54	0.79
(9,8)	3.89	-0.17	0.35	0.67
(11,10)	3.15	-0.12	0.26	0.58
(13,12)	2.64	-0.09	0.21	0.52

angle of approximately $\theta = 21^\circ$. Our value for $\theta = 21.78^\circ$ is 1.3 eV, which is, indeed, a discrepancy of around 18%. This difference is anticipated when utilizing DFT, which underestimates the Fermi velocity of graphene by about 15% because of the lack of many-body effects, as shown by Hedin's *GW* approximation (*GW*) calculations [47]. Also in Table II, the ΔE_{VHS} values are displayed, which were accessed through optical measurements [28], which are also in good agreement with our results. In both cases, differences are expected because of both DFT and measurement accuracies, including the experimental estimation of θ .

APPENDIX B: GAPS CLOSE TO THE DIRAC CONES

Here, we focus on studying the gaps discussed above, and their corresponding VHSs as a function of θ , by inspecting the DOS of different TBLG systems in Fig. 8(a). For comparison, we also include the DOS of pristine G. The electronic gaps are identified by the depletion in the DOS (solid curves) compared with pristine G (dashed curves). For $\theta = 21.78^\circ$, the first empty and occupied VHSs are at about +1.2 and -1.3 eV, respectively, with an energy difference, ΔE_{VHS} , of about 2.5 eV. A systematic decrease in ΔE_{VHS} is found, as θ also decreases. Before, we mentioned that these two gaps which originate the DOS peaks are close to **K**. Moreover, the π -band dispersion depends on the relative angle between layers, inducing a variation of the charge-carrier group velocity. We particularly find a reduction in the group velocity along the Γ -**K** direction, as $\theta \rightarrow 0^\circ$. Figure 8(b) shows the EEB for TBLG with $\theta = 21.78^\circ, 9.43^\circ, 6.01^\circ$, and 3.89° for k points near **K** approaching from Γ . Notice that spectral weights also change as a function of θ , becoming smaller when $\theta \rightarrow 0^\circ$, meaning that the interlayer interaction is stronger at small angles. The slope of the linear dispersion adjacent to **K** changes, meaning a reduction in the Fermi velocity v_F of the charge carriers. This reduction has been previously reported [14,38,48]. For the largest θ , the slope change is minimal compared with pristine G. So far, we have shown that the electronic properties in TBLG depend on the interlayer interaction of $2p_z$ orbitals, which can be modulated with the angle between layers. The coupling is more significant as the moiré superlattice area is large. These results are summarized in Table II and Fig. 8(b), where it is clearly shown that ΔE_{11} and v_F tend to zero as $\theta \rightarrow 0^\circ$. This latter leads to the localization of Dirac electrons in regions with AA stacking in real space [48], while at such energies TBLGs behave more likely as pristine G layers when $\theta \rightarrow 30^\circ$, as the interaction is small. These results are in agreement with other models [49,50].

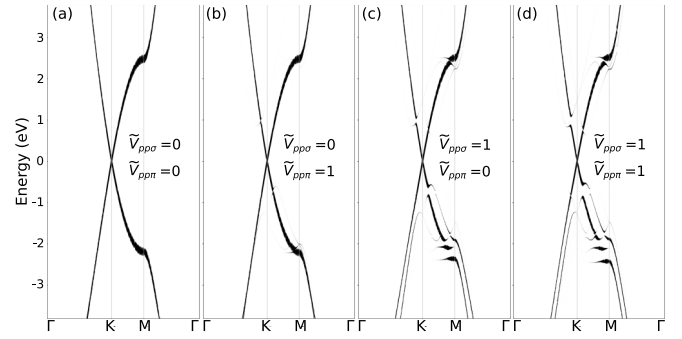


FIG. 9. Effect of different interlayer interaction parameters based on the tight-binding model for TBLG (4,3) with $\theta = 9.43^\circ$. The reduced parameters are defined in terms of the fitted values (starred): $\tilde{V}_{pp\sigma} = V_{pp\sigma}/V_{pp\sigma}^*$; $\tilde{V}_{pp\pi} = V_{pp\pi}/V_{pp\pi}^*$.

APPENDIX C: TIGHT-BINDING MODEL

The tight-binding model used here is formulated within the Slater-Koster approach, considering only p_z orbitals. For both in-plane and out-of-plane interactions, we assumed an exponential distance dependence, $\exp(-\alpha(\frac{d}{d_0} - 1))$, where d is the distance between different atoms and $d_0^{\text{in}} = 1.42 \text{ \AA}$ is the first-neighbors distance between in-plane atoms. In comparison, the first-neighbors distance between out-of-plane atoms is $d_0^{\text{out}} = 3.35 \text{ \AA}$. Interactions of type σ and π between p_z orbitals are considered for both sublattices and among them (Fig. 9). The parameters were fitted to Hamiltonian elements after the DFT self-consistent field (SCF) Hamiltonian “Wannierization” [51], being thus an orthogonal model. The in-plane hopping parameters are

$$V_{pp\pi}^{AA} = 0.8316 \text{ eV}, \quad V_{pp\pi}^{AB} = -2.89 \text{ eV}, \quad V_{pp\sigma}^{AB} = -2.89 \text{ eV},$$

$$\alpha^{AA} = 1.70, \quad \alpha^{AB} = 2.60, \quad \text{and} \quad d_0^{\text{in}} = 1.42 \text{ \AA}.$$

Note that in-plane interactions of type $V_{pp\sigma}$ are always null since the cosine director is zero. The out-of-plane parameters are

$$V_{pp\sigma}^{AA'} = 0.299 \text{ eV}, \quad V_{pp\pi}^{AA'} = -1.035 \text{ eV},$$

$$V_{pp\sigma}^{AB'} = 0.268 \text{ eV}, \quad V_{pp\pi}^{AB'} = -0.819 \text{ eV};$$

$$\text{here, } \alpha^{AA'} = \alpha^{AB'} = 8.1 \quad \text{and} \quad d_0^{\text{out}} = 3.35 \text{ \AA}.$$

- [1] G. R. Bhimanapati, Z. Lin, V. Meunier, Y. Jung, J. C. S. Das, D. Xiao, Y. Son, M. S. Strano, V. R. Cooper, L. Liang, S. G. Louie, E. Ringe, W. Zhou, S. S. Kim, R. R. Naik, B. G. Sumpter, H. Terrones, F. Xia, Y. Wang *et al.*, *ACS Nano* **9**, 11509 (2015).
- [2] K. S. Novoselov, A. Mishchenko, A. Carvalho, and A. H. Castro Neto, *Science* **353**, aac9439 (2016).

- [3] A. K. Geim and I. V. Grigorieva, *Nature (London)* **499**, 419 (2013).
- [4] Y. Cao, V. Fatemi, S. Fang, K. Watanabe, T. Taniguchi, E. Kaxiras, and P. Jarillo-Herrero, *Nature (London)* **556**, 43 (2018).
- [5] Y. Cao, V. Fatemi, A. Demir, S. Fang, S. L. Tomarken, J. Y. Luo, J. D. Sanchez-Yamagishi, K. Watanabe, T. Taniguchi, E.

- Kaxiras, R. C. Ashoori, and P. Jarillo-Herrero, *Nature (London)* **556**, 80 (2018).
- [6] M. Yankowitz, S. Chen, H. Polshyn, Y. Zhang, K. Watanabe, T. Taniguchi, D. Graf, A. F. Young, and C. R. Dean, *Science* **363**, 1059 (2019).
- [7] T. Georgiou, R. Jalil, B. D. Belle, L. Britnell, R. V. Gorbachev, S. V. Morozov, Y.-J. Kim, A. Gholinia, S. J. Haigh, O. Makarovskiy, L. Eaves, L. A. Ponomarenko, A. K. Geim, K. S. Novoselov, and A. Mishchenko, *Nat. Nanotechnol.* **8**, 100 (2013).
- [8] L. Britnell, R. V. Gorbachev, R. Jalil, B. D. Belle, F. Schedin, A. Mishchenko, T. Georgiou, M. I. Katsnelson, L. Eaves, S. V. Morozov, N. M. R. Peres, J. Leist, A. K. Geim, K. S. Novoselov, and L. A. Ponomarenko, *Science* **335**, 947 (2012).
- [9] F. Hidalgo, A. Rubio-Ponce, and C. Noguez, *J. Phys. Chem. C* **123**, 15273 (2019).
- [10] Y. Wang, Z. Ni, L. Liu, Y. Liu, C. Cong, T. Yu, X. Wang, D. Shen, and Z. Shen, *ACS Nano* **4**, 4074 (2010).
- [11] W. Landgraf, S. Shallcross, K. Türschmann, D. Weckbecker, and O. Pankratov, *Phys. Rev. B* **87**, 075433 (2013).
- [12] Z. Wang, Q. Chen, and J. Wang, *J. Phys. Chem. C* **119**, 4752 (2015).
- [13] K. Kim, A. DaSilva, S. Huang, B. Fallahazad, S. Larentis, T. Taniguchi, K. Watanabe, B. J. LeRoy, A. H. MacDonald, and E. Tutuc, *Proc. Natl. Acad. Sci. USA* **114**, 3364 (2017).
- [14] I. Brihuega, P. Mallet, H. González-Herrero, G. Trambly de Laissardi re, M. M. Ugeda, L. Magaud, J. M. G mez-Rodr guez, F. Yndur  n, and J.-Y. Veuillen, *Phys. Rev. Lett.* **109**, 196802 (2012).
- [15] C.-J. Kim, A. S  nchez-Castillo, Z. Ziegler, Y. Ogawa, C. Noguez, and J. Park, *Nat. Nanotechnol.* **11**, 520 (2016).
- [16] R. Bistritzer and A. H. MacDonald, *Phys. Rev. B* **84**, 035440 (2011).
- [17] B. Hunt, J. D. Sanchez-Yamagishi, A. F. Young, M. Yankowitz, B. J. LeRoy, K. Watanabe, T. Taniguchi, P. Moon, M. Koshino, P. Jarillo-Herrero, and R. C. Ashoori, *Science* **340**, 1427 (2013).
- [18] G. Li, A. Luican, J. L. Dos Santos, A. C. Neto, A. Reina, J. Kong, and E. Andrei, *Nat. Phys.* **6**, 109 (2010).
- [19] Z. Wang, D. Ki, H. Chen, H. Berger, A. H. MacDonald, and A. F. Morpurgo, *Nat. Commun.* **6**, 8339 (2015).
- [20] A. V. Rozhkov, A. O. Sboychakova, A. L. Rakhmanov, and F. Nori, *Phys. Rep.* **648**, 1 (2016).
- [21] H. Yang, A. Liang, C. Chen, C. Zhang, N. B. Schroeter, and Y. Chen, *Nat. Rev. Mater.* **3**, 341 (2018).
- [22] Z. Y. Rong and P. Kuiper, *Phys. Rev. B* **48**, 17427 (1993).
- [23] T. Ohta, J. T. Robinson, P. J. Feibelman, A. Bostwick, E. Rotenberg, and T. E. Beechem, *Phys. Rev. Lett.* **109**, 186807 (2012).
- [24] S. Lisi, X. Lu, T. Benschop *et al.*, *Nat. Phys.* **17**, 189 (2021).
- [25] R. W. Havener, H. Zhuang, L. Brown, R. G. Hennig, and J. Park, *Nano Lett.* **12**, 3162 (2012).
- [26] R. He, T.-F. Chung, C. Delaney, C. Keiser, L. A. Jauregui, P. M. Shand, C. C. Chancey, Y. Wang, J. Bao, and Y. P. Chen, *Nano Lett.* **13**, 3594 (2013).
- [27] A. Tejeda, *J. Phys. D: Appl. Phys.* **50**, 351001 (2017).
- [28] P. Moon and M. Koshino, *Phys. Rev. B* **87**, 205404 (2013).
- [29] F. S  nchez-Ochoa, F. Hidalgo, M. Pruneda, and C. Noguez, *J. Phys.: Condens. Matter* **32**, 025501 (2020).
- [30] L. Li and M. Zhao, *J. Phys. Chem. C* **118**, 19129 (2014).
- [31] P. Ordej  n, E. Artacho, and J. M. Soler, *Phys. Rev. B* **53**, R10441(R) (1996).
- [32] J. M. Soler, E. Artacho, J. D. Gale, A. Garc  a, J. Junquera, P. Ordej  n, and D. S  nchez-Portal, *J. Phys.: Condens. Matter* **14**, 2745 (2002).
- [33] G. Rom  n-P  rez and J. M. Soler, *Phys. Rev. Lett.* **103**, 096102 (2009).
- [34] J. Klime  , D. R. Bowler, and A. Michaelides, *J. Phys.: Condens. Matter* **22**, 022201 (2009).
- [35] N. Troullier and J. L. Martins, *Phys. Rev. B* **43**, 1993 (1991).
- [36] H. J. Monkhorst and J. D. Pack, *Phys. Rev. B* **13**, 5188 (1976).
- [37] K. Momma and F. Izumi, *J. Appl. Crystallogr.* **44**, 1272 (2011).
- [38] K. Uchida, S. Furuya, J.-I. Iwata, and A. Oshiyama, *Phys. Rev. B* **90**, 155451 (2014).
- [39] N. Ashcroft and N. Mermin, *Solid State Physics* (Saunders College, Philadelphia, 1976).
- [40] J. Hermann, R. A. DiStasio, and A. Tkatchenko, *Chem. Rev. (Washington, DC)* **117**, 4714 (2017).
- [41] S. Zhao, P. Moon, Y. Miyauchi, T. Nishihara, K. Matsuda, M. Koshino, and R. Kitaura, *Phys. Rev. Lett.* **124**, 106101 (2020).
- [42] K. Liu, C. Jin, X. Hong, J. Kim, A. Zettl, E. Wang, and F. Wang, *Nat. Phys.* **10**, 737 (2014).
- [43] D. Novko and M. Kralj, *npj 2D Mater. Appl.* **3**, 48 (2019).
- [44] F. Wu, A. H. MacDonald, and I. Martin, *Phys. Rev. Lett.* **121**, 257001 (2018).
- [45] B. Lian, Z. Wang, and B. A. Bernevig, *Phys. Rev. Lett.* **122**, 257002 (2019).
- [46] J. Yin, H. Wang, H. Peng, Z. Tan, L. Liao, L. Lin, X. Sun, A. L. Koh, Y. Chen, H. Peng, and Z. Liu, *Nat. Commun.* **7**, 10699 (2016).
- [47] P. E. Trevisanutto, C. Giorgetti, L. Reining, M. Ladisa, and V. Olevano, *Phys. Rev. Lett.* **101**, 226405 (2008).
- [48] G. T. De Laissardi re, D. Mayou, and L. Magaud, *Nano Lett.* **10**, 804 (2010).
- [49] G. Trambly de Laissardi re, D. Mayou, and L. Magaud, *Phys. Rev. B* **86**, 125413 (2012).
- [50] J. M. B. Lopes dos Santos, N. M. R. Peres, and A. H. Castro Neto, *Phys. Rev. B* **86**, 155449 (2012).
- [51] G. Pizzi, V. Vitale, R. Arita, S. Blugel, F. Freimuth, G. G ranton, M. Gibertini, D. Gresch, C. Johnson, T. Koretsune, J. Iba  ez-Azpiroz, H. Lee, J.-M. Lihm, D. Marchand, A. Marrazzo, Y. Mokrousov, J. I. Mustafa, Y. Nohara, Y. Nomura, L. Paulatto *et al.*, *J. Phys.: Condens. Matter* **32**, 165902 (2020).